

A stellar flare—coronal mass ejection event revealed by X-ray plasma motions

C. Argiroffi^{1,2*}, F. Reale^{1,2}, J. J. Drake³, A. Ciaravella², P. Testa³, R. Bonito², M. Miceli^{1,2}, S. Orlando^{1,2} and G. Peres^{1,2}

Coronal mass ejections (CMEs), often associated with flares^{1–3}, are the most powerful magnetic phenomena occurring on the Sun. Stars show magnetic activity levels up to ten thousand times higher⁴, and CME effects on stellar physics and circumstellar environments are predicted to be substantial^{5–9}. However, stellar CMEs remain observationally unexplored. Using time-resolved high-resolution X-ray spectroscopy of a stellar flare on the active star HR 9024 observed with the High Energy Transmission Grating Spectrometer onboard the Chandra X-ray Observatory space telescope, we distinctly detected Doppler shifts in S xv, Si xiv and Mg xii lines that indicate upward and downward motions of hot plasmas (around 10–25 MK) within the flaring loop, with velocities of 100–400 km s^{−1}, in agreement with a model of a flaring magnetic tube. Most notably, we also detected a later blueshift in the O viii line that reveals an upward motion, with velocity 90 ± 30 km s^{−1}, of cool plasma (about 4 MK), that we ascribe to a CME coupled to the flare. From this evidence we were able to derive a CME mass of $1.2_{-0.8}^{+2.6} \times 10^{21}$ g and a CME kinetic energy of $5.2_{-3.6}^{+27.7} \times 10^{34}$ erg. These values provide clues in the extrapolation of the solar case to higher activity levels in other stars, suggesting that CMEs could indeed be a major cause of mass and angular momentum loss.

Intense stellar magnetic fields are responsible for the so-called stellar magnetic activity^{4,10}, and for the associated highly energetic phenomena occurring in the outer stellar atmosphere. CMEs, the most energetic coronal phenomena, are observed only on the Sun, because their detection and identification needs spatial resolution.

CMEs are closely linked to flares³. In the standard scenario¹¹, flares are driven by impulsive magnetic reconnections in the corona. The released energy is transported along the magnetic field lines and heats the underlying chromosphere, which expands upward at hundreds of kilometres per second, filling the overlying magnetic structure (flare rising phase). Then this plasma gradually cools down radiatively and conductively (flare decay). The flare magnetic drivers often also cause large-scale expulsions of previously confined plasma, CMEs, that carry away large amounts of mass and energy. Solar observations demonstrate that CME occurrence, mass and kinetic energy increase with increasing flare energy^{1,2}, corroborating the links between flares and CMEs.

Active stars have stronger magnetic fields, higher flare energies and hotter and denser coronal plasma¹². Their activity levels, measured by the X-ray to bolometric luminosity ratio, L_X/L_{bol} , can be up to 10,000 times higher than the solar level. Currently, the properties of stellar CMEs can only be presumed by extrapolating the solar flare–CME relation up to several orders of magnitude higher,

even though active stellar coronae differ profoundly from the Sun's corona. This extrapolation suggests that stellar CMEs should cause enormous amounts of mass and kinetic energy loss^{6–9} (up to about $10^{-9} M_{\odot} \text{ yr}^{-1}$ and about $0.1 L_{\text{bol}}$, respectively, where M_{\odot} is the solar mass), and could strongly influence exoplanets⁵.

Thus far, there have been a few claims of stellar CME observations. Blueshifted components of chromospheric lines have sometimes been attributed to CMEs^{13–15}, but these could also be explained by chromospheric brightenings or evaporation events^{16,17}. CMEs have been invoked to explain increased X-ray absorption observed during flares¹⁸. However, the simultaneous variations of flare temperature and emission measure¹⁸ (EM) imply that the increased absorption may be a spurious result, coming from the limited diagnostic power of low-resolution X-ray spectroscopy, combined with the oversimplified assumptions of an isothermal flaring plasma and a constant quiescent corona. CMEs have also been invoked to explain transient ultraviolet and X-ray absorptions observed in the eclipsing precataclysmic binary system V471 Tau¹⁹. However, such absorptions can equally be produced by a stellar wind²⁰. In addition to their ambiguous interpretations, none of these candidate detections provide the required CME physical properties, unless substantial assumptions are made.

We present here strong evidence for the detection and identification of a stellar CME, an estimate of its properties, and the simultaneous monitoring of the associated flare energetics. In the Sun, a flare–CME event produces hot plasma moving upward and downward within the flaring loop, and, after the flare onset, cool plasma in the CME moving upward. Therefore, monitoring the plasma velocity at different temperatures during a stellar flare is a potentially powerful method of searching for CMEs. The unrivalled X-ray spectral resolution of the Chandra High Energy Transmission Grating Spectrometer (HETGS), combined with detailed hydrodynamic modelling, allowed us to investigate the strong flare²¹ observed on the active star HR 9024.

HR 9024 is a G1 III single giant star²², with stellar mass $M_{\star} \approx 2.85 M_{\odot}$ and stellar radius $R_{\star} \approx 9.45 R_{\odot}$, located at 139.5 pc. Its convective envelope and rotational period²³ (24.2 days) indicate that an efficient dynamo is at work²², as is expected in single G-type giants²⁴. Even if some contribution to its magnetic field may have a fossil origin²², HR 9024 shows coronal properties²¹ ($L_X \approx 10^{31}$ erg s^{−1}, with $T \approx 1$ –100 MK) and magnetic-field properties²² (a dominant poloidal field with $B_{\text{max}} \approx 10^2$ G) analogous to that of other active stars. Therefore, irrespective of the origin of some magnetic components, and bearing in mind that active stars may show diverse magnetic configurations, the coronal phenomena occurring on HR 9024 can be considered as representative of those of active stars.

¹Department of Physics and Chemistry, University of Palermo, Palermo, Italy. ²INAF - Osservatorio Astronomico di Palermo, Palermo, Italy. ³Smithsonian Astrophysical Observatory, Cambridge, MA, USA. *e-mail: costanza.argiroffi@unipa.it

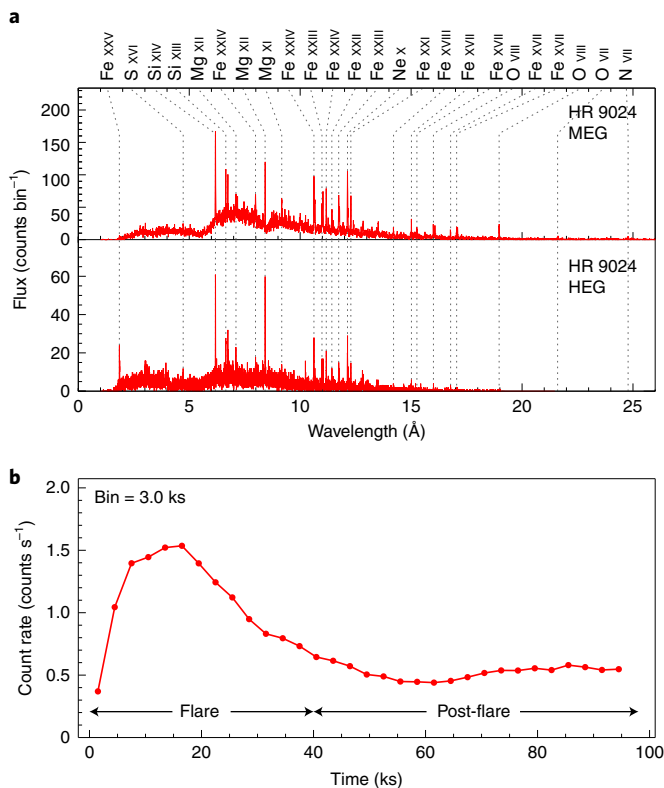


Fig. 1 | Observed X-ray spectra and light curve of HR 9024. **a**, X-ray spectra collected with the Medium Energy Grating (MEG) and High Energy Grating (HEG) during the 98-ks-long Chandra observation, with the strongest emission lines labelled. MEG and HEG bin sizes are 5 mÅ and 2.5 mÅ. **b**, X-ray light curve registered during the Chandra observation, obtained from the +1 and -1 diffraction order spectra of HEG and MEG.

The HR 9024 X-ray spectrum was collected during a 98-ks-long Chandra/HETGS observation (Fig. 1a), in which a strong flare (peak luminosity of about 10^{32} erg s $^{-1}$ and X-ray fluence of about 10^{36} erg) was registered (Fig. 1b).

The high energy of this flare maximizes the probability of its having an associated CME¹. The flaring loop located near the stellar disk centre, as implied by the Fe fluorescence²⁵, maximizes the possibility of detecting the radial velocities of both the flaring and CME plasmas.

We measured time-resolved individual line positions, considering only strong and isolated lines that probe plasma with temperature T ranging from 2 to 25 MK (Fig. 2 and Methods and Supplementary Table 1). We found:

- Significant blueshifts during the rising phase of the flare in the S xvi line at 4.73 Å (-400 ± 180 km s $^{-1}$) and in the Si xiv line at 6.18 Å (-270 ± 120 km s $^{-1}$), with a 99.99% combined significance of the two lineshifts;
- Significant redshifts in the Si xiv line at 6.18 Å (140 ± 80 km s $^{-1}$) and the Mg xii line at 8.42 Å (70 ± 50 and 90 ± 40 km s $^{-1}$), during the maximum and decay phases of the flare, with a 99.997% combined significance of the three lineshifts; and
- A significant blueshift in the O viii line at 18.97 Å (-90 ± 30 km s $^{-1}$), after the flare, significant at the 99.9% level.

The first two Doppler shifts tell us that hot flaring plasma moves upward at the beginning of the flare, and then settles back down to the chromosphere, as predicted¹. We compared the observed velocities with predictions based on the flaring loop model²¹ (Methods

and Supplementary Fig. 1). For each line and each time interval, we computed the radial velocity corresponding to the predicted line centroid, for different possible inclinations of the flaring loop (identified by the ϕ and θ angles defined in Fig. 3a).

The best agreement between observed and predicted velocities (Fig. 3b–f) is obtained assuming a loop observed from above ($\phi = 0^\circ$ and $\theta = 90^\circ$; see Methods), confirming previous independent results²⁵. The agreement for the Si xiv and Mg xii lines is striking (Fig. 3c–f). The observed S xvi blueshift, associated with chromospheric plasma upflows, is of the same order but even more extended in time than expected. The agreement obtained for flaring plasma velocities is an important validation of the standard flare model for flare energies up to 10^{36} erg.

Interestingly, we found that the coolest line inspected, O viii Ly α , which forms at about 3 MK, is strongly blueshifted (with $v = -90 \pm 30$ km s $^{-1}$) in the post-flare phase, whereas no shift is observed during the flare. The low rotational velocity of HR 9024 ($v \sin i \approx 20$ km s $^{-1}$)²³ excludes the possibility that this motion is due to structures fixed on the stellar surface.

We identify this motion as the signature of a CME (Fig. 3g): it involves only cool plasma, it occurs after a strong flare located near the stellar disk centre, and the observed velocity is within the range of solar CME velocities³ (that is, 20–3,000 km s $^{-1}$). Solar flares are sometimes also followed by the formation of expanding giant arches²⁶. However, this expansion is very slow (around 1–10 km s $^{-1}$) and possibly only apparent because of the sequential brightening of different loops²⁷, and hence cannot be related to Doppler shifts. Although the extrapolation of the magnetic configuration of the Sun to more active stars is not straightforward, a CME remains the most logical and (at present) only explanation.

Hypothesizing that the CME moves exactly along the line of sight, the distance travelled by the CME in the post-flare phase is about $0.8R_*$. Most probably the CME started its motion at the same time as the flare onset (solar flare and CME onsets differ by most 1 ks, and the O viii profile during the flare appears to be broad, with some blue-shifted excess; see Fig. 2f). Assuming a constant velocity, the total distance travelled by the CME is around $1.4R_*$. At this distance from the stellar surface the escape velocity is 220 km s $^{-1}$, larger by a factor of about 2.4 than the CME velocity. The real CME velocity, as well as its travelled distance, could be higher because of the possible inclination between the CME trajectory and the line of sight. Assuming an inclination of 45° (that is, the maximum separation angle for solar flare–CME pairs^{1,2}) the ratio between the local escape velocity and the real CME velocity would reduce to around 1.6.

The initial CME mechanical energy has, however, a minor importance in determining the end of the CME. Solar CMEs follow non-ballistic motions. Magnetic forces and wind interactions often cause strong outward acceleration up to heights of several solar radii³. The detected CME on HR 9024 indeed shows an approximately constant velocity during the post-flare phase (-100 ± 50 km s $^{-1}$ and -80 ± 50 km s $^{-1}$ in the 40–70-ks and 70–98-ks time intervals, respectively), indicating that strong magnetic forces act on the CME, balancing the stellar gravity. Having no data to follow the CME after the end of the Chandra observation, we cannot firmly conclude whether the CME does eventually escape to infinity.

Assuming that the post-flare O viii line comes entirely from the CME, and inferring a CME temperature of 4 ± 1 MK, we derive an EM of $(2.8 \pm 1.0) \times 10^{53}$ cm $^{-3}$ (see Methods and Supplementary Table 2). As in hot plasmas of solar CMEs, we expect that the CME plasma is optically thin and that, in the observed interval, there is no strong heating source²⁸. The duration of the observed CME X-ray emission (stable in the post-flare phase) indicates a radiative cooling time of $\tau > 60$ ks. Conservatively, we assumed $\tau \approx 200$ ks and a factor of 10 for its confidence interval (that is, $60 \text{ ks} < \tau < 600 \text{ ks}$). From that we inferred the CME density (n_e), volume (V), mass (M),

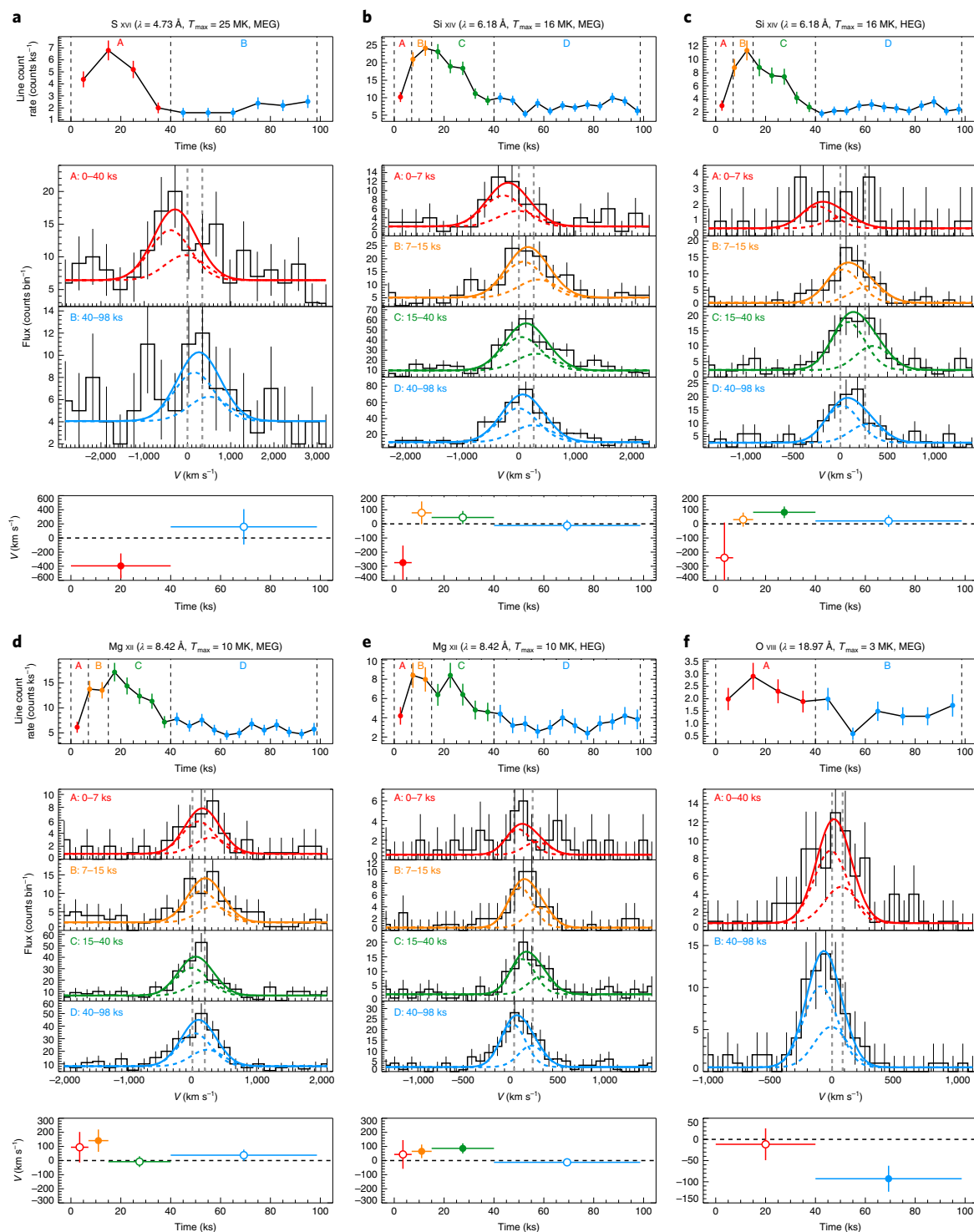


Fig. 2 | Time-resolved line fits. **a**, Analysis of the S xvi line at 4.73 Å, as registered with the MEG ± 1 orders. In all plots vertical bars indicate errors at 1σ . The top panel shows the count rate detected in a 0.1 Å interval centred on the line. Letters and colours indicate the different time intervals used to collect the line profile. The middle panel shows the observed line profile, in different time intervals (black), with the corresponding best-fit function superimposed (in different colours, following the same colour-code used for the different time intervals, with dashed curves corresponding to the two transitions of the Ly α doublet, and the solid curve corresponding to their sum). Vertical dashed grey lines mark the rest positions of the two Ly α components. On the x axis we report the velocity in the stellar reference frame with respect to the bluest Ly α component. The bottom panel shows line Doppler shifts, in the different time intervals, computed in the stellar reference frame. Horizontal bars specify the time interval. Filled circles mark velocities different from zero at the 1σ level at least, open circles indicate velocities compatible with zero. The other plots analogously show the time-resolved analysis of: the Si xiv line at 6.18 Å as registered with MEG (**b**) and HEG (**c**), the Mg xii line at 8.42 Å as registered with MEG (**d**) and HEG (**e**), and the O viii line at 18.97 Å as registered with MEG (**f**).

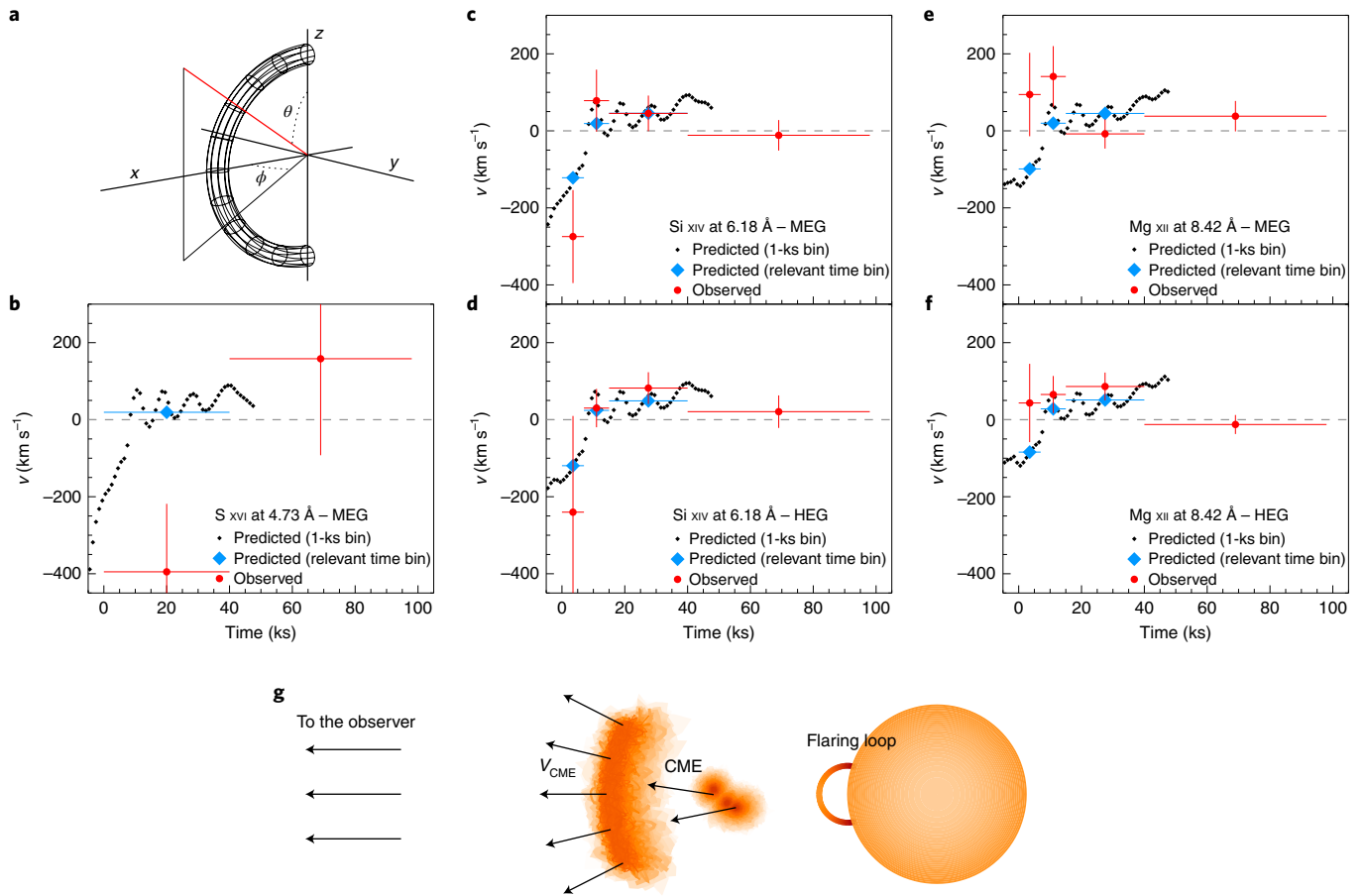


Fig. 3 | Comparison between observed and predicted velocities. **a**, Viewing geometry of the flaring loop with respect to the observer direction (red line) identified by the ϕ and θ angles. **b–f**, Comparison between the line Doppler shifts observed (red circles) and those predicted by the flare model, for $\phi=0^\circ$ and $\theta=90^\circ$, for the lines showing significant shifts. Small dark diamonds indicate velocities predicted in 1-ks intervals. Large blue diamonds mark predicted velocities computed integrating the model spectra over the same time intervals considered for the observed spectra. Vertical bars indicate errors at 1σ . Horizontal bars mark the time interval duration. **g**, Schematic illustration of the star/loop/CME configuration.

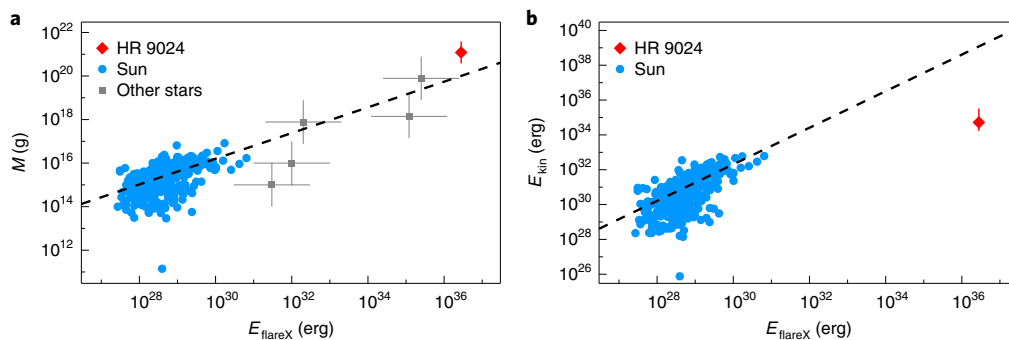


Fig. 4 | Extrapolation of the solar flare–CME relation. The mass M (**a**) and kinetic energy E_{kin} (**b**) of solar CMEs are shown as a function of the X-ray fluence of the associated flares¹, with the corresponding power-law relations², compared to the analogous properties of the observed flare–CME pair on HR 9024, and that of other candidate stellar CMEs⁹.

and kinetic energy (E_{kin}) (see Methods and Supplementary Table 2), to obtain:

$$n_e = (5.5_{-3.7}^{+11.8}) \times 10^8 \text{ cm}^{-3}$$

$$V = (1.1_{-1.0}^{+10.3}) \times 10^{36} \text{ cm}^3$$

$$M = (1.2_{-0.8}^{+2.6}) \times 10^{21} \text{ g}$$

$$E_{\text{kin}} = (5.2_{-3.6}^{+27.7}) \times 10^{34} \text{ erg}$$

Computing also the X-ray flare fluence ($E_{\text{flareX}} \approx 2.8 \times 10^{36} \text{ erg}$), we can compare this flare–CME pair with the solar ones (Fig. 4).

The inferred CME mass suggests that the correlation with the flare energy, observed for the Sun^{6,7}, might hold also for stronger flares at higher activity levels. Despite their unsettled identification (as CMEs or as chromospheric evaporation), unconstrained mass estimate (the reported values are lower limits⁹), and lack of X-ray coverage (X-ray flare fluence was assumed to be comparable to that in the U band⁹), the previous candidate stellar CMEs⁹ (grey squares in Fig. 4a) also agree with this high-energy extrapolation. Conversely, the obtained CME kinetic energy is about 10,000 less than expected from solar-data extrapolations (Fig. 4b).

Therefore, CMEs of active stars may not be a scaled version of solar CMEs. In terms of the amount of mass ejected, the CME formation mechanism appears to scale smoothly from the solar case to higher flare energies and higher magnetic activity levels. In terms of kinematics, remembering that solar CMEs can experience acceleration both in the low corona ($<1R_{\odot}$ from the solar surface) or at large distances³, the CME acceleration mechanism appears instead to be less efficient, possibly suggesting a different energy partition in the flare–CME pair.

These CME parameters (that is, a mass compatible with solar extrapolations, and a significantly reduced E_{kin}) fit well with magnetohydrodynamic models^{29,30}. This indicates that the balance between the magnetic forces acting on the CME can be different on active stars, with the ratio between the inward force, due to the magnetic tension of the overlying large-scale field, and the outward force, due to the magnetic pressure of the flux rope, being higher in active stars than in the Sun.

As an integrated effect, assuming that the observed CME eventually escapes the star, the inferred large CME mass supports the hypothesis that CMEs can be a major cause of mass and angular momentum loss in active stars^{6–9}, even if it remains unclear down to what energy flares can cause eruptions in active stars. The diminished E_{kin} to E_{flareX} ratio indicates instead that, at high activity levels, the energy fraction carried away from the star by CMEs diminishes. That supports the idea that magnetic activity can at most extract a thousandth of the stellar bolometric luminosity, excluding the huge magnetic energy budget implied by solar-case extrapolations to higher activity levels⁷.

Methods

Data analysis. HR 9024 was observed on August 2001 for 98 ks with Chandra/HETGS (ObsID 1892). This instrument configuration consists of two transmission gratings, the HEG and the MEG, used with the ACIS-S detector. The two gratings simultaneously collect spectra in the 1.2–15 Å (HEG) and 2.5–31 Å (MEG) intervals, with a spectral resolution (full-width at half-maximum, FWHM) of 12 mÅ and 23 mÅ, respectively. In this work we inspected the HEG and MEG spectra of HR 9024 separately, each one obtained by adding +1 and –1 diffraction orders. The data were obtained from the Grating-Data Archive and Catalog³¹.

The wavelength calibration of the Chandra/HETGS allows velocity measurements down to a few tens of kilometres per second by comparing line positions within and between observations, as confirmed by several studies^{32–35}. Hence the Chandra/HETGS is well suited to measuring the velocity of flaring and CME plasmas.

To search for Doppler shifts we selected a sample of strong and isolated emission lines (Supplementary Table 1). Inspecting isolated lines allows us to avoid line position uncertainties caused by line blending. Moreover, monitoring individual lines, instead of inspecting the whole spectrum, allows us to probe plasma components separately at different temperatures. The selected line sample is composed of: the Lyman series lines of N VII, O VIII, Mg XII, Si XIV and S XVI; the He-like ion lines of Mg XI, Si XIII and O VII; and the strong Fe XVII lines in the 15–17 Å range. We did not inspect the Ne IX and Ne X lines, because of their severe blendings with Fe lines. The maximum formation temperature of the inspected line sample ranges from 2 MK to 25 MK.

We determined the position of each selected line by least-squares fitting its observed profile over different time intervals. The selected duration of the inspected time intervals is aimed at: (1) separating the phases corresponding to substantially different predicted velocities (the hydrodynamic model, described below and in Supplementary Fig. 1, predicts high upward velocity during the rising phase and slower downward motions during the maximum and decay phases; see Fig. 3b–f); and (2) collecting enough counts to perform the line fit. For each line we performed the fit in a small wavelength interval, with a width of about

0.1–0.2 Å, around the line's rest wavelength. As a best-fit function we assumed a Gaussian plus a constant, to take the continuum emission into account as well. The σ of the Gaussian was fixed to the predicted value³². Since the Ly α lines are doublets, we fitted their observed profiles with two Gaussians, with relative positions fixed to the predicted wavelength difference, and relative intensity fixed to the predicted value (that is 2:1 in the optically thin emission regime).

The observed lineshifts, with respect to the predicted wavelengths, allow us to calculate the velocity with respect to the Chandra satellite reference frame (v_{sat}). We assumed that these calculated velocities are the same as those with respect to the Earth, because the satellite velocity is low (at most 1–2 km s^{–1} with respect to the Earth). We computed the plasma velocity in the stellar reference frame as $v = v_{\text{sat}} + v_{\text{E}} - v_{*}$, where v_{E} is the line-of-sight Earth velocity at the epoch of the observation (that is, $v_{\text{E}} = 19.9$ km s^{–1} in the heliocentric reference frame), and v_{*} is the radial velocity of HR 9024 (that is, $v_{*} = -1.6$ km s^{–1} in the heliocentric reference frame). Throughout the paper we indicated outward motions with respect to us (redshifts) with positive radial velocities, and inward motions with respect to us (blueshifts) with negative radial velocities.

The lines shown in Fig. 2 and discussed in the paper are the ones for which a largeshift was detected in at least one time interval. For lines with a high enough signal-to-noise (S/N) ratio, we analysed both HEG and MEG spectra. Because of the different S/N and spectral resolution between corresponding MEG and HEG spectra (with MEG providing higher S/N but lower spectral resolution than HEG), large lineshifts were sometimes found in only one grating. In these cases, the shift measurements obtained with the two gratings (even if only one was notably different from zero) were nevertheless compatible among themselves.

We display in Supplementary Fig. 2 the observed and predicted shifts for those lines with a S/N high enough to allow time-resolved spectral fitting, for which no large shift was obtained. For the hottest of these lines (that is, the Si XIII line at 6.65 Å, and the Mg XII line at 7.11 Å), the expected radial velocities during the flare evolution are high enough to be detectable with the Chandra gratings. However, the low S/N collected for these lines (total line counts are listed in Supplementary Table 1) avoids precise shift measurements and/or prevents from us exploring time bins short enough. For the coolest of these latter lines (that is, all the Fe XVII lines), in addition to the low S/N , much smaller shifts in only very short time intervals are expected. We note that the large redshifted velocities of about 200 km s^{–1} expected for the very last part of the flare correspond to phases in which the line fluxes become negligible, because of the vanishing EM value of the flaring loop.

Flaring loop model and line emission synthesis. To infer the expected line Doppler shifts due to plasma motions during the flare, and to constrain the loop orientation with respect to the observer, we considered the flare loop model presented by Testa et al.²¹. This model assumes that the stellar magnetic field is so strong as to confine the plasma inside single closed magnetic tubes (coronal loops); that the footpoints of the flaring loop are anchored to the photosphere; that the flaring plasma moves and transports energy only along the field lines; and that its evolution can be described with a one-dimensional hydrodynamic model along the tube. The hydrodynamic equations for a compressible plasma fluid are solved numerically to obtain the evolution of the plasma density, temperature and velocity along the loop. The flare is triggered with a strong heat pulse injected inside an initially hydrostatic and relatively cool loop atmosphere, which includes a tenuous corona linked to a dense chromosphere. Tuning the model parameters to reproduce the observed evolution of T and EM during the flare, we obtained a total loop length of 5×10^{11} cm; the duration and rate of the heat pulse to be 15 ks and 1.2×10^{33} erg s^{–1}, respectively, for a total injected energy of about 1.7×10^{37} erg; and that the pulse heats the plasma to a maximum temperature of about 150 MK, making it expand from the chromosphere at a maximum speed of about 1,800 km s^{–1}, which drops rapidly below 400 km s^{–1} after a few kiloseconds since the heat pulse started. The evolution of velocity, temperature and EM of the flaring loop are shown in Supplementary Fig. 1.

The X-ray emission of the flaring loop is assumed to be optically thin. Line emissivities were retrieved from the APED database³⁶. We computed line emission from the flaring loop considering both short time intervals (1 ks, to monitor line profiles on timescales corresponding to the characteristic timescales of the flaring loop variability) and long time intervals (corresponding to that adopted for the observed line profiles) to perform a proper comparison between observed and predicted lineshifts.

We computed predicted line profiles for different viewing geometries of the loop, exploring the range $0^{\circ} < \phi < 90^{\circ}$ and $0^{\circ} < \theta < 90^{\circ}$ (Fig. 3a). The ϕ angle determines a global scaling factor in the predicted lineshifts, with $\phi \approx 0^{\circ}$ corresponding to the largest shifts, and $\phi \approx 90^{\circ}$ corresponding to no shift. Taking the possible values of θ into account, and considering that the footprint portions of the loop are responsible for the highest emission and highest velocity (Supplementary Fig. 1), configurations with $\theta \approx 90^{\circ}$ maximize the lineshifts, while configurations with $\theta \approx 0^{\circ}$ minimize the lineshifts (causing also some line broadening, because of the simultaneous redshifted and blueshifted contributions originating in the motions of plasma located near the loop apex). We found that only for $\phi = 0^{\circ}$ and $\theta = 90^{\circ}$ are the predicted shifts large enough to reproduce what is observed.

In general, since the coronal part of the loop comprises most of the flaring volume, filled with upflowing plasma at temperatures ≥ 50 –100 MK, we would

expect Doppler shifts in highly ionized lines, such as Ca xx, formed at around 50 MK, but these are not detected²¹. Instead, we detected Doppler shifts associated with motions of flaring plasma, in lines at $T \approx 10\text{--}25$ MK (hence emitted mostly at the loop footpoints). This happens because Doppler shift measurements are best obtained in lines detected with high S/N ratio. The spatial distributions of T and EM along the flaring loop mean that hotter lines, mainly emitted by higher loop portions where the EM is lower, have lower S/N than cooler lines, mainly emitted by lower loop portions where the EM is higher.

Finally, the agreement obtained between observed and predicted velocities, considering that this hydrodynamic flare model was tuned to match only X-ray flux and plasma temperature, supports the hypothesis of a flare occurring in a single loop, and allows us to confirm the loop geometry, the temporal and spatial distribution of heating, and the kinetic energy budget involved in plasma motions.

Cool plasma velocity after the flare. The blueshifted emission, detected at the 3σ level in the post-flare phases in the O VIII line, is robust because of the accuracy of the Chandra wavelength calibration: in a sample of active stars³² the shift displayed by this line is always smaller than 13 km s^{-1} . To further corroborate this detection we inspected the N VII Ly α line at 24.78 \AA , which forms mainly at 2 MK. This line does not have enough counts to fit its profile. Selecting the post-flare interval, the average position of the photons detected in the $\pm 1,000 \text{ km s}^{-1}$ interval around its rest position is $-110 \pm 80 \text{ km s}^{-1}$, thus confirming the cool plasma blueshift at the 1.4σ level. These two simultaneous blueshifts further support the implications of the detected plasma motion. To summarize, considering all the inspected lines in the post-flare phase, the plasma at $T \lesssim 4 \text{ MK}$ moves upward, and hence it is located in the CME, possibly representing its hottest component; conversely, plasma with $T \gtrsim 5 \text{ MK}$ appears to be motionless, and hence it is situated in stable coronal structures.

CME parameter estimation. Assuming that the O VIII emission is entirely due to a CME, we have a direct measurement of the CME average radial velocity, v , and of the CME total luminosity in the O VIII line, $L_{\text{O VIII}}$, corrected for the interstellar absorption³⁷ of $4 \times 10^{20} \text{ cm}^{-2}$. To infer the temperature T of the CME we considered the observed post-flare line ratio between the O VII resonance line at 21.60 \AA and the O VIII Ly α line. This ratio provides a lower limit³⁶ of 3 MK for T . In addition, the Fe XVII lines, which form mainly at 5 MK, do not show any blueshift, indicating that they are produced by coronal loops and not by the CME. We therefore deduced that the CME temperature T should be $4 \pm 1 \text{ MK}$. We do not detect any large decline in the O VIII line flux. This suggests that the CME probably moves as a coherent structure, without experiencing significant adiabatic expansion, in spite of the large distance travelled in the related time range.

The line luminosity, together with the plasma temperature, allow us to determine the CME emission measure EM to be:

$$EM = \frac{L_{\text{O VIII}}}{A_{\text{O}} G(T)}$$

where $G(T)$ is the line emissivity function (APED database³⁶), and A_{O} is the oxygen abundance (we adopted the abundances inferred from the post-flare emission²¹).

The CME emission is observed for about 60 ks. Therefore, its radiative cooling time τ must be longer. We assumed $\tau = 200 \text{ ks}$, with a confidence interval of a factor of 10, that corresponds to $60 \text{ ks} < \tau < 600 \text{ ks}$. By also assuming that, during the observed emission, there is no heating source in the CME, that its emission is optically thin, and that the hydrogen to electron density ratio $n_{\text{H}}/n_{\text{e}}$ is 0.83 (value corresponding to high-temperature plasma with cosmic abundances), we can estimate the CME electron density from:

$$E_{\text{int}} = \frac{3}{2} (n_{\text{e}} + n_{\text{H}}) V k_{\text{B}} T$$

$$\dot{E}_{\text{rad}} = n_{\text{e}} n_{\text{H}} V \Lambda(T)$$

$$\tau = \frac{E_{\text{int}}}{\dot{E}_{\text{rad}}} \Rightarrow n_{\text{e}} = \frac{3}{2} \left(\frac{n_{\text{e}}}{n_{\text{H}}} + 1 \right) \frac{k_{\text{B}} T}{\tau \Lambda(T)}$$

where E_{int} is the CME internal energy, \dot{E}_{rad} is the radiative loss rate, V is the CME volume, and $\Lambda(T)$ is the radiative loss function per EM unit in the $1\text{--}2,000 \text{ \AA}$ wavelength interval, computed assuming the plasma emissivities of the APED database³⁶. The estimates for EM and n_{e} finally allow us to derive the volume V , mass M and kinetic energy E_{kin} of the CME:

$$V = \frac{EM}{n_{\text{e}} n_{\text{H}}}$$

$$M = V n_{\text{H}} m = \frac{EM}{n_{\text{e}}} m$$

$$E_{\text{kin}} = \frac{1}{2} M v^2$$

where m is the mean mass per hydrogen atom. All the values of the relevant CME parameters are reported in Supplementary Table 2.

In the estimation of the uncertainty of n_{e} , V , M , and E_{kin} , we considered only the uncertainty on τ , because it is much larger than the uncertainties on T and EM. Only in the computation of the upper limit of the confidence interval of E_{kin} did we include also a factor related to the possible flare–CME separation angle, in agreement with solar observations^{1,2} that indicate separations of at most 45° . The observed O VIII line does not show much broadening in the post-flare interval; its width is in fact compatible with the instrumental width. Therefore, velocity dispersion along the line of sight in the CME plasma is expected to be small ($\leq 100 \text{ km s}^{-1}$), further corroborating the inferred E_{kin} value. Finally, we note that both M and E_{kin} are directly proportional to τ . Therefore, the strict lower limit of 60 ks, provided by the stable post-flare emission in the O VIII, corresponds to the lower limits of the confidence intervals of M and E_{kin} . Conversely, the already large upper limit on M is an a posteriori confirmation of the adopted upper limit on τ . Moreover, the reasonable assumptions made for the τ confidence interval are also supported by the inferred n_{e} value, neatly compatible with the density observed in solar CMEs^{28,38,39}.

Data availability

The Chandra dataset analysed in this work (ObsID 1892) can be accessed from <http://cxc.harvard.edu/>. The data that support plots and findings of this study are available from the corresponding author upon reasonable request.

Received: 27 July 2018; Accepted: 12 April 2019;

Published online: 27 May 2019

References

- Yashiro, S. & Gopalswamy, N. Statistical relationship between solar flares and coronal mass ejections. In *Universal Heliophysical Processes* (eds Gopalswamy, N. & Webb, D. F.) Vol. 257, 233–243 (IAU Symp., 2009).
- Aarnio, A. N., Stassun, K. G., Hughes, W. J. & McGregor, S. L. Solar flares and coronal mass ejections: a statistically determined flare flux–CME mass correlation. *Sol. Phys.* **268**, 195–212 (2011).
- Webb, D. F. & Howard, T. A. Coronal mass ejections: observations. *Living Rev. Sol. Phys.* **9**, 3 (2012).
- Wright, N. J., Drake, J. J., Mamajek, E. E. & Henry, G. W. The stellar-activity–rotation relationship and the evolution of stellar dynamos. *Astrophys. J.* **743**, 48 (2011).
- Khodachenko, M. L. et al. Coronal mass ejection (CME) activity of low mass M stars as an important factor for the habitability of terrestrial exoplanets. I. CME impact on expected magnetospheres of Earth-like exoplanets in close-in habitable zones. *Astrobiology* **7**, 167–184 (2007).
- Aarnio, A. N., Matt, S. P. & Stassun, K. G. Mass loss in pre-main-sequence stars via coronal mass ejections and implications for angular momentum loss. *Astrophys. J.* **760**, 9 (2012).
- Drake, J. J., Cohen, O., Yashiro, S. & Gopalswamy, N. Implications of mass and energy loss due to coronal mass ejections on magnetically active stars. *Astrophys. J.* **764**, 170 (2013).
- Osten, R. A. & Wolk, S. J. Connecting flares and transient mass-loss events in magnetically active stars. *Astrophys. J.* **809**, 79 (2015).
- Odert, P., Leitinger, M., Hanslmeier, A. & Lammer, H. Stellar coronal mass ejections. I. Estimating occurrence frequencies and mass-loss rates. *Mon. Not. R. Astron. Soc.* **472**, 876–890 (2017).
- Noyes, R. W., Hartmann, L. W., Baliunas, S. L., Duncan, D. K. & Vaughan, A. H. Rotation, convection, and magnetic activity in lower main-sequence stars. *Astrophys. J.* **279**, 763–777 (1984).
- Shibata, K. & Magara, T. Solar flares: magnetohydrodynamic processes. *Living Rev. Sol. Phys.* **8**, 6 (2011).
- Güdel, M. X-ray astronomy of stellar coronae. *Annu. Rev. Astron. Astrophys.* **12**, 71–237 (2004).
- Houdebine, E. R., Foing, B. H. & Rodono, M. Dynamics of flares on late-type dM stars. I. Flare mass ejections and stellar evolution. *Astron. Astrophys.* **238**, 249–255 (1990).
- Vida, K. et al. Investigating magnetic activity in very stable stellar magnetic fields. Long-term photometric and spectroscopic study of the fully convective M4 dwarf V374 Pegasi. *Astron. Astrophys.* **590**, A11 (2016).
- Vida, K. et al. The quest for stellar coronal mass ejections in late-type stars. I. Investigating Balmer-line asymmetries of single stars in virtual observatory data. *Astron. Astrophys.* **623**, A49 (2019).
- Gunn, A. G., Doyle, J. G., Mathioudakis, M., Houdebine, E. R. & Avgoloupis, S. High-velocity evaporation during a flare on AT Microscopii. *Astron. Astrophys.* **285**, 489–496 (1994).
- Berdyugina, S. V., Ilyin, I. & Tuominen, I. The active RS Canum Venaticorum binary II Pegasi. III. Chromospheric emission and flares in 1994–1996. *Astron. Astrophys.* **349**, 863–872 (1999).
- Moschou, S.-P., Drake, J. J., Cohen, O., Alvarado-Gomez, J. D. & Garraffo, C. A monster CME obscuring a coronal star flare. *Astrophys. J.* **850**, 191 (2017).

19. Wheatley, P. J. ROSAT observations of V471 Tauri, showing that stellar activity is determined by rotation, not age. *Mon. Not. R. Astron. Soc.* **297**, 1145–1150 (1998).
20. Mullan, D. J., Sion, E. M., Bruhweiler, F. C. & Carpenter, K. G. Evidence for a cool wind from the K2 dwarf in the detached binary V471 Tauri. *Astrophys. J. Lett.* **339**, L33–L36 (1989).
21. Testa, P., Reale, F., Garcia-Alvarez, D. & Huenemoerder, D. P. Detailed diagnostics of an X-ray flare in the single giant HR 9024. *Astrophys. J.* **663**, 1232–1243 (2007).
22. Borisova, A. et al. The different origins of magnetic fields and activity in the Hertzsprung gap stars, OU Andromedae and 31 Comae. *Astron. Astrophys.* **591**, A57 (2016).
23. Strassmeier, K. G., Serkowitz, E. & Granzer, T. Starspot photometry with robotic telescopes, UVB(RI)_c and by light curves of 47 active stars in 1996/97. *Astron. Astrophys. Suppl. Ser.* **140**, 29–53 (1999).
24. Pizzolato, N., Maggio, A. & Sciortino, S. Evolution of X-ray activity of 1–3 M_{sun} late-type stars in early post-main-sequence phases. *Astron. Astrophys.* **361**, 614–628 (2000).
25. Testa, P. et al. Geometry diagnostics of a stellar flare from fluorescent X-rays. *Astrophys. J.* **675**, L97 (2008).
26. Švestka, Z. Speeds of rising post-flare structures. *Sol. Phys.* **169**, 403–413 (1996).
27. West, M. J. & Seaton, D. B. SWAP observations of post-flare giant arches in the long-duration 14 October 2014 solar eruption. *Astrophys. J. Lett.* **801**, L6 (2015).
28. Landi, E., Raymond, J. C., Miralles, M. P. & Hara, H. Physical conditions in a coronal mass ejection from hinode, stereo, and SOHO observations. *Astrophys. J.* **711**, 75–98 (2010).
29. Drake, J. J., Cohen, O., Garraffo, C. & Kashyap, V. Stellar flares and the dark energy of CMEs. In *Solar and Stellar Flares and their Effects on Planets* (eds. Kosovichev, A. G., Hawley, S. L. & Heinzel, P.) Vol. 320, 196–201 (IAU Symp., 2016).
30. Alvarado-Gómez, J. D., Drake, J. J., Cohen, O., Moschou, S. P. & Garraffo, C. Suppression of coronal mass ejections in active stars by an overlying large-scale magnetic field: a numerical study. *Astrophys. J.* **862**, 93 (2018).
31. Huenemoerder, D. P. et al. TGCat: the Chandra transmission grating data catalog and archive. *Astron. J.* **141**, 129 (2011).
32. Argiroffi, C. et al. Redshifted X-rays from the material accreting onto TW Hydrae: evidence of a low-latitude accretion spot. *Astron. Astrophys.* **607**, A14 (2017).
33. Brickhouse, N. S., Dupree, A. K. & Young, P. R. X-ray Doppler imaging of 44i Bootis with Chandra. *Astrophys. J.* **562**, L75–L78 (2001).
34. Chung, S. M., Drake, J. J., Kashyap, V. L., Lin, L. W. & Ratzlaff, P. W. Doppler shifts and broadening and the structure of the X-ray emission from Algol. *Astrophys. J.* **606**, 1184–1195 (2004).
35. Ishibashi, K., Dewey, D., Huenemoerder, D. P. & Testa, P. Chandra/HETGS observations of the Capella system: the primary as a dominating X-ray source. *Astrophys. J.* **644**, L117–L120 (2006).
36. Smith, R. K., Brickhouse, N. S., Liedahl, D. A. & Raymond, J. C. Collisional plasma models with APEC/APED: emission-line diagnostics of hydrogen-like and helium-like ions. *Astrophys. J.* **556**, L91–L95 (2001).
37. Singh, K. P., Drake, S. A., White, N. E. & Simon, T. ROSAT observations of five chromospherically active stars. *Astron. J.* **112**, 221 (1996).
38. Cheng, X., Zhang, J., Saar, S. H. & Ding, M. D. Differential emission measure analysis of multiple structural components of coronal mass ejections in the inner corona. *Astrophys. J.* **761**, 62 (2012).
39. Landi, E., Miralles, M. P., Raymond, J. C. & Hara, H. Hot plasma associated with a coronal mass ejection. *Astrophys. J.* **778**, 29 (2013).

Acknowledgements

We acknowledge a modest financial contribution from the ASI-INAF agreement n.2017-14.H.O.

Author contributions

C.A., F.R., J.J.D., A.C., P.T., R.B., M.M., S.O. and G.P. contributed to scientific discussion and writing of the text. C.A. and J.J.D. contributed to analysis of observational data. F.R. contributed to the hydrodynamic model development, and C.A. to the synthesis of the model line profile.

Competing interests

The authors declare no competing interests.

Additional information

Supplementary information is available for this paper at <https://doi.org/10.1038/s41550-019-0781-4>.

Reprints and permissions information is available at www.nature.com/reprints.

Correspondence and requests for materials should be addressed to C.A.

Peer review information: *Nature Astronomy* thanks Krisztian Vida and the other, anonymous, reviewer(s) for their contribution to the peer review of this work.

Publisher's note: Springer Nature remains neutral with regard to jurisdictional claims in published maps and institutional affiliations.

© The Author(s), under exclusive licence to Springer Nature Limited 2019